nature physics

LETTERS

https://doi.org/10.1038/s41567-022-01719-4

Check for updates

Coherence enhancement of solid-state qubits by local manipulation of the electron spin bath

Wentian Zheng[1,8], Ke Bian[1,8] ✉, Xiakun Chen[1], Yang Shen[2], Shichen Zhang[1], Rainer Stöhr[3,4], Andrej Denisenko[3,4], Jörg Wrachtrup[3,4], Sen Yang[2] ✉ and Ying Jiang[1,5,6,7] ✉

The performance of qubit-based technologies can be strongly limited by environmental sources of noise and disorder that cause decoherence. Qubits used in quantum sensing are usually very close to the host surface to enhance their coupling to external targets. This leaves them vulnerable to the effects of the surrounding noisy electron spin bath near the surface, which is very challenging to eliminate. Here we developed an efficient method to engineer the immediate electrostatic environment of nitrogen vacancy centre qubits located several nanometres beneath the diamond surface. We adopt a 'pull-and-push' strategy for near-surface charge manipulation using the strong local electric field of an atomic force microscope tip. Our technique is particularly effective for extremely shallow nitrogen vacancy centres, increasing their spin echo time by up to 20 fold. This corresponds to an 80-fold enhancement in the potential sensitivity for detecting individual external proton spins. Our work not only represents a step towards overcoming a fundamental restriction to applications of shallow nitrogen vacancy centres for quantum sensing but may also provide a general route for enhancing the coherence of solid-state qubits.

The nitrogen vacancy (NV) centre hosted in diamond, a prototype solid-state spin qubit, has emerged as one of the most promising candidates for quantum sensing because of its long coherent times even at ambient conditions[1,2]. In recent years, the ultrahigh sensitivity of such quantum sensors has made them ideal for detecting nuclear spins and electron spins at nanoscale[3–5,13–15]. In addition, the NV centre has also been demonstrated as a powerful probe for magnetometry[16–18], electrometry[19,20], thermometry[21,22] and biosensors[23,24] in a wide range of applications. Based on detecting the interactions between external signals and its spin states, the ultimate sensitivity of NV centres is primarily determined by the quantum coherence[25–27]. To enhance the coupling strength of NVs to external parameters and achieve high signal-to-noise ratios, it is crucial to bring the NVs into proximity to the diamond surface. However, due to the ever-present magnetic/electric noise near the diamond surface after the NV growth and surface treatments, shallow NVs suffer greatly from various decoherence processes[6–8,28]. Therefore, there is a fundamental trade-off between growing shallow NVs and preserving their coherence or sensitivity, leading to a great challenge for NV-based quantum sensing and other quantum technologies. To date, a compromise has had to be made between the depth of NVs used for sensing (typically ~5 nm) and the achievable coherence time (T_2, typically ~10 μs).

Because the yield to produce shallow NVs is only ~1% for low-energy implantation (5 keV in our case), a large quantity of defects such as nitrogen atoms (P1 centres) and vacancy complexes are inevitably generated in the immediate neighbourhood of the NV centres even when using optimized recipes[29–31], leading to a high density of unpaired electrons near the diamond surface, which is the dominant source of decoherence. Previous efforts to protect the coherence of NVs have mainly focused on the manipulation and engineering of the quantum states of NVs by using microwave pulse sequences[9–12]. However, these passive methods are not so effective for shallow NVs owing to their strong coupling with the immense electron spin noise. Therefore, an ideal approach would be to directly target the source of the problem, that is, to physically eliminate the near-surface unpaired electrons that continuously produce fluctuating noise.

In this work, we successfully developed a new method based on a qPlus-type atomic force microscope (AFM) system[32,33] under ambient conditions, where a sharp conductive tip was used to locally manipulate the charges near single NVs. Through the strong local electric field assisted with the laser excitation, the immediate electrostatic environment of the shallow NV was actively purified through the 'pull-and-push' strategy for charge manipulation, leading to a notable enhancement of T_2. We emphasize that this method is particularly effective for shallow NVs (depth <5 nm) with poor coherence ($T_2 < 10$ μs). For example, for a shallow NV with depth of ~2 nm, we improved the T_2 time from 1.3 to 26 μs (a 20-fold enhancement), corresponding to an 80-fold sensitivity enhancement when detecting incoherent signals from external elements such as proton clusters[3,4,13,14]. Through a general noise analysis protocol, we found that our method can suppress both the surface and subsurface spin noise, which is different from previous works merely focused on eliminating electron spin noise on the surface[10].

The experiments were performed inside a home-built qPlus-based AFM system[20], where a tungsten tip was sharpened by using a focused ion beam (FIB) (see Methods for details). We focused on shallow NVs with a depth of several nanometres, generated by using an implantation energy of 5 keV through a thin boron-doped layer[30]. Using such a technique, the subsurface vacancy complexes are greatly suppressed during NV generation, leading to high-quality NVs with improved coherent properties (Methods).

[1]International Center for Quantum Materials, School of Physics, Peking University, Beijing, P. R. China. [2]Department of Physics, The Hong Kong University of Science and Technology, Hong Kong, P. R. China. [3]3rd Institute of Physics, University of Stuttgart and Institute for Quantum Science and Technology (IQST), Stuttgart, Germany. [4]Max Planck Institute for Solid State Research, Stuttgart, Germany. [5]Interdisciplinary Institute of Light-Element Quantum Materials and Research Center for Light-Element Advanced Materials, Peking University, Beijing, P. R. China. [6]Collaborative Innovation Center of Quantum Matter, Beijing, P. R. China. [7]CAS Center for Excellence in Topological Quantum Computation, University of Chinese Academy of Sciences, Beijing, P. R. China. [8]These authors contributed equally: Wentian Zheng, Ke Bian. ✉e-mail: bian.k@pku.edu.cn; phsyang@ust.hk; yjiang@pku.edu.cn

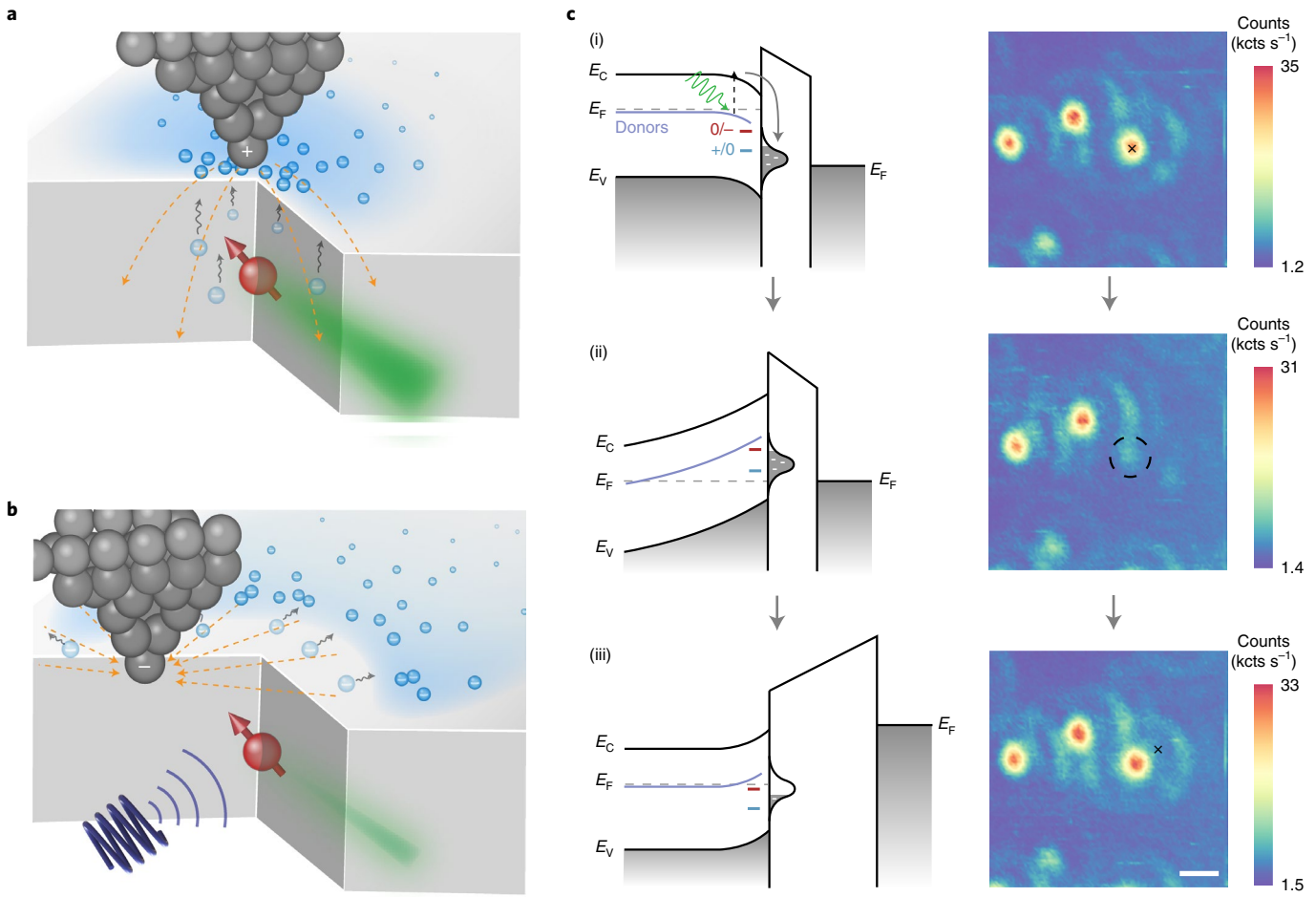

Fig. 1 | The 'pull-and-push' strategy for charge manipulation near the NV by using the local electric field of an AFM tip. a, Schematic showing the process of donor ionization and subsequent surface polarization. A conductive tip (grey balls) with positive bias is approached close to the single NV centre (red ball). Paramagnetic spins such as unpaired electrons (blue balls) are ionized under a strong 532 nm laser, pulled (wavy arrows) towards the diamond surface through the local electric field (dashed arrows) and finally trapped on the surface. **b**, Schematic showing the process of pushing the electrons (blue balls) trapped on the diamond surface. The tip (grey balls) with negative bias is positioned several hundred nanometres laterally away from the same NV (red ball). At the same time, the microwave pulses (bottom left) and weak 532 nm laser (green ray) are turned on for spin-echo measurements. **c**, The band diagrams and corresponding confocal images under the 'pull-and-push' charge manipulation. (i) Under positive bias, the selected NV remains in the NV^- state through the tip-induced band bending effect, with the diamond surface negatively polarized. The charge transition levels of NV^+/NV^0 and NV^0/NV^- are denoted by short blue and red lines, respectively. The charge transition level of the paramagnetic spins is denoted by the purple line. (ii) After the surface polarization, the accumulation of the electrons at the surface results in a large built-in electric field, which depletes NV^- into the NV^+ state (dashed circle). (iii) The negatively biased tip pushes the surface-trapped electrons away from the NV. In this case, the built-in electric field is weakened and the NV^+ recovers to NV^-, while a large amount of the paramagnetic spins near the NV still remains depleted. E_F is the Fermi level. E_C and E_V denote the edges of the conduction and valance band, respectively. Scale bar 500 nm. The tip position is marked by a black cross in the confocal images.

In the following, we show that this method can further enhance the coherence time of shallow NVs in this state-of-the-art sample by engineering the electrostatic environment in a well-controlled manner.

Our technique basically consists of two steps to manipulate the surrounding charges of NVs (Fig. 1). First, we approached the tip to the vicinity of a selected single NV centre with a positive bias voltage (typically larger than +50 V) (Fig. 1a,c,i) and polarized the surface by pulling the unpaired electrons of charged defects in the bulk onto the surface with the assistance of 532 nm laser excitation (typically 300–400 μW, see Methods for details). During this process, such subsurface defects are photo-ionized to produce free carriers, which are transported under the strong local electric field from the tip and are finally captured by the surface traps. The dynamics of the surface polarization is on the microsecond order (Supplementary Fig. 1 and Supplementary Text 1), with a typical polarized area of ~265 × 265 nm^2 (Methods). After retracting the tip, the extracted electrons are trapped in surface/interfacial states, leading to a built-in electric field[20] which is strong enough to deplete NV^- into NV^+ (Fig. 1c,ii). Such a surface polarization state is long-lived, indicating that these surface/interfacial states are deep within the diamond bandgap (Supplementary Fig. 2). For the next step, we moved the tip several hundred nanometres horizontally away from the NV^+ and continuously applied a negative voltage (typically larger than −50 V) during the measurements. In this case, those surface-trapped electrons were pushed away from the NV centre. As a result, the NV^+ recovered to NV^- (Fig. 1b) because of the weakened built-in electric field (Fig. 1c, iii). To achieve T_2 enhancement under a fixed negative bias, the tip should be positioned within a suitable region in the 'pushing' step (Extended Data Fig. 1 and Methods). On the one hand, the tip should not be positioned horizontally within ~300 nm of the NV centre, since the large

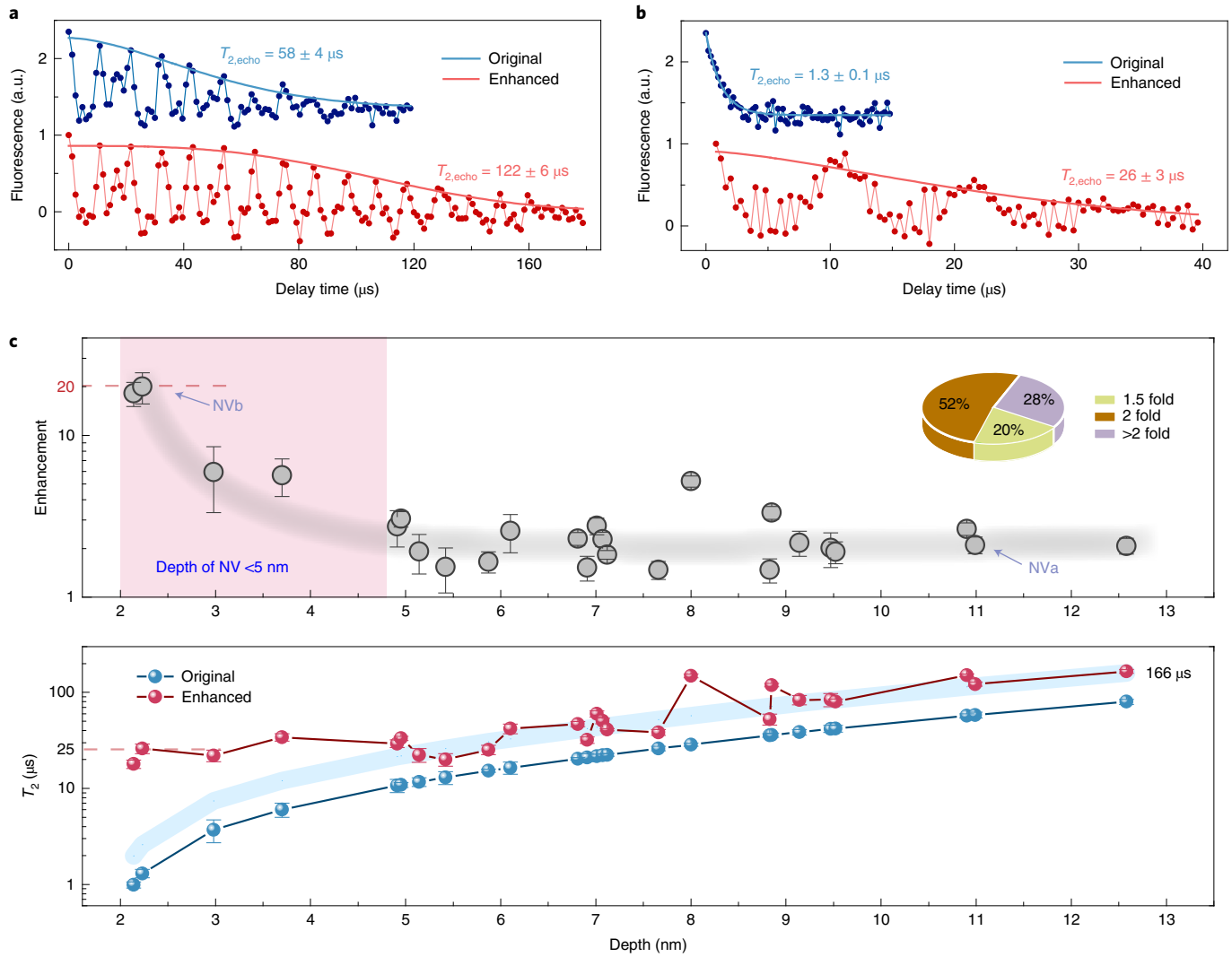

Fig. 2 | The coherence enhancement after charge manipulation. a, Spin echo measurements demonstrating a two-fold T_2 enhancement from 58 ± 4 μs to 122 ± 6 μs. More collapses and revivals appear at the longer delay time after the charge manipulation (red curve). Laser power 70 μW, bias voltage −60 V. **b**, Spin echo measurements showing a 20-fold T_2 enhancement from 1.3 ± 0.1 μs to 26 ± 3 μs. Laser power 70 μW, bias voltage −320 V. The decayed envelope of the spectra in **a** and **b** are fitted by $C = \exp(-(\tau/T_2)^n)$. Spectra in **a** and **b** are measured under ~175 G and offset vertically for clarity. The value for the bias voltage chosen in the 'pushing' step depends on the specific depth of the NV and the density of the paramagnetic spins in its neighbourhood. One can choose the optimized bias voltage according to the largest T_2 enhancement. **c**, A summary of 25 shallow NV centres with enhanced coherence. The *x* axis is the estimated NV depth based on the original T_2 according to the model described in Methods. Upper: coherence enhancement versus NV depth. The inset indicates that about 80% of the NVs show a T_2 enhancement of two fold or above. The grey line is a guide to the eye. The NVs in **a** and **b** are labelled 'NVa' and 'NVb', respectively. Lower: the corresponding T_2 of the same NVs as measured by the spin echo technique. The faded blue curve denotes two-fold enhancement of the original T_2. It is clear that the NVs with smaller depth (below 5 nm, highlighted in the upper panel) show larger coherence enhancement. The maximum T_2 we obtained is 166 ± 8 μs. Most of the NVs show T_2 values longer than 25 μs after charge manipulation, which is a notable value for shallow NV-based quantum sensing.

negative electric field would induce strong upward band bending, leading again to a change of the NV^- into NV^+. On the other hand, when the tip is micrometres away from the NV, the field strength is insufficient to push surface electrons efficiently. Therefore, we can clean up the unpaired electrons surrounding the NV centre by using such a 'pull-and-push' method.

Figure 2a shows typical spin echo measurements of a NV centre before (blue) and after (red) the 'pull-and-push' charge manipulation. More collapses and revivals induced by the ^{13}C nuclear spin bath[2] clearly appeared in the spin echo spectra $C(T_2)$ of the manipulated NV. By fitting the envelope, we found that the original T_2 of 58 ± 4 μs was enhanced to 122 ± 6 μs. Strikingly, the short T_2 of a low-quality NV can be improved to 20-fold longer, from ~1.3 ± 0.1 μs to 26 ± 3 μs (Fig. 2b). Based on the calibration of the T_2 versus the depth of NV through double electron electron resonance (DEER) (Extended Data Fig. 2 and Methods)[34], such a low-quality NV may lie in proximity to the diamond surface within only ~2 nm and thus suffers from stronger coupling with the surrounding paramagnetic spins. Generally, our method was highly efficient for shallow NVs as long as the sharpness and cleanness of the tips are ensured (Supplementary Fig. 3, Supplementary Table 1 and Supplementary Text 2).

Figure 2c summarizes the results for 25 shallow NV centres showing coherence enhancement beyond the fitting errors, among which the longest T_2 achieved was 166 ± 8 μs. This value is notable for NVs with a depth of several nanometres. About 80% of the

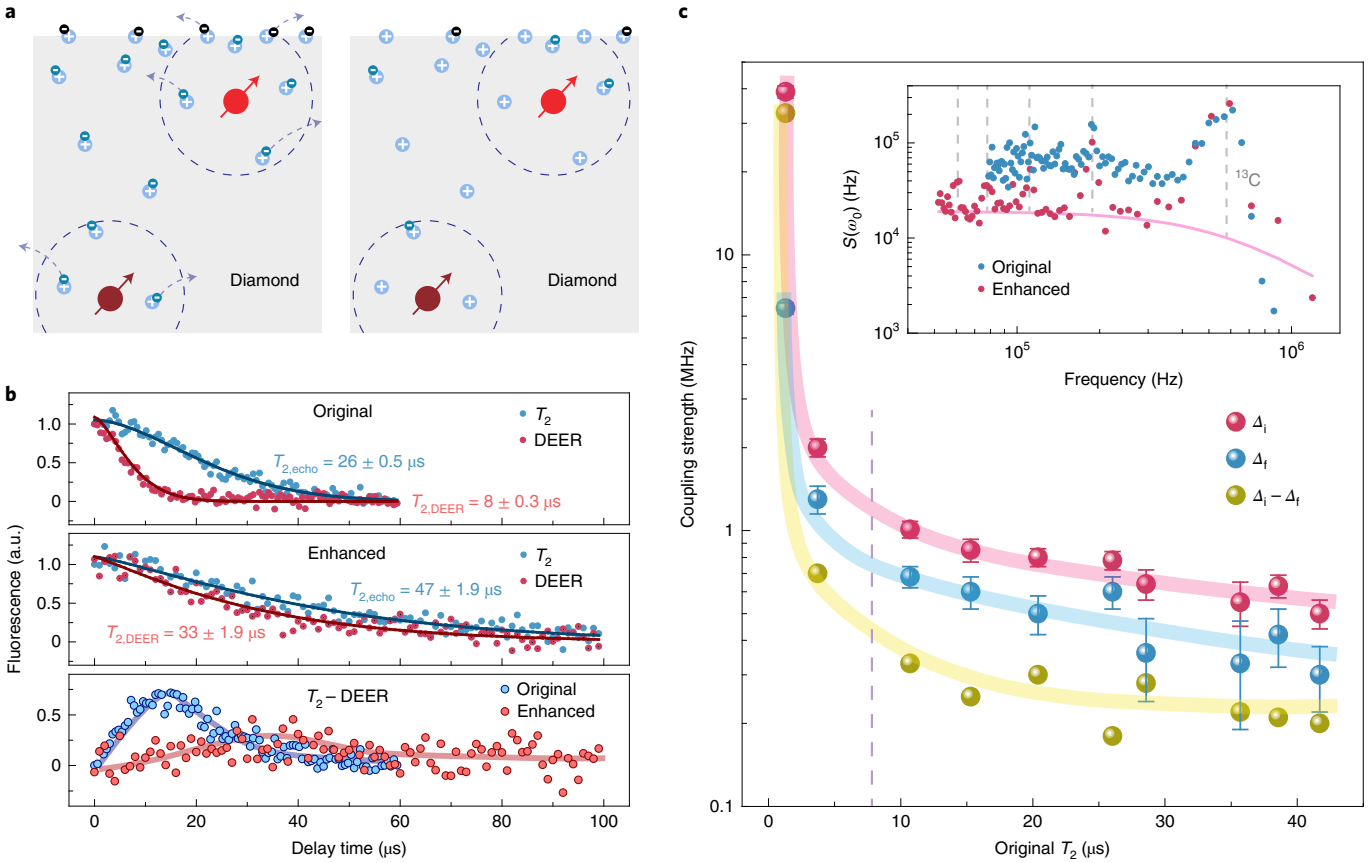

Fig. 3 | Noise analyses using DEER and the spectral decomposition technique. a, Schematic showing the electron spin noise around a single NV (red dots). During the charge manipulation, the unpaired electrons on/beneath (black/blue) the diamond surface are efficiently depleted, leading to suppressed spin noise. The dashed circles represent the region where the spin noise dominates the decoherence of the NVs. **b**, DEER and spin echo spectra before (upper) and after (middle) charge manipulation. The solid lines are fits by $C = \exp(-(\tau/T_2)^n)$. Lower: the difference between the spin echo and DEER signals. Solid curves are guides to the eye. **c**, The coupling strength of different NVs with the surrounding electron spin bath versus their original T_2. We extracted the coupling strength by fitting the noise spectra. The increased Δ_i and Δ_f values at shorter T_2 result from the increased coupling strength with the surface spins. The differential coupling strength $\Delta_i - \Delta_f$ shows a weak dependence for NVs with T_2 longer than 10 μs (dashed line) but a large variation for NVs with extremely poor coherence. The coloured bands are guides to the eye. Inset: Typical noise spectra before and after charge manipulation. A substantial suppression of noise is clearly visualized. ω_0 is the frequency of noise spectra. The dashed lines mark the peaks corresponding to $f_L/(2k-1)$, $k = 1, 2, 3\ldots$, where $f_L = 551.92$ kHz is the Larmor frequency of the residual ^{13}C spins bath. All the data in **c** were measured under 515.6 G.

measured NV centres show a coherence enhancement above two fold (Fig. 2c, upper panel, inset). Plotting T_2 and the T_2 enhancement as functions of the NV depth (Fig. 2c) reveals that the T_2 enhancement is close to two fold at depths larger than 5 nm, while the NVs with depth <5 nm demonstrate notably larger T_2 enhancements. Therefore, our method works particularly well for extremely shallow NVs, which are surrounded by high-density paramagnetic defects near the surface. It is worth noting that the T_2 values of about 90% of the measured shallow NVs were improved to above 25 μs (Fig. 2c, lower panel).

To gain further insight into the mechanism of coherence enhancement, we performed a detailed noise analysis. For shallow NVs, the sources of spin noise can generally be divided into two regimes, corresponding to surface (black) and subsurface noise (blue) (Fig. 3a). The noise on the diamond surface is mainly attributed to surface defects[31] or adsorption layers. For shallow NVs prepared by our method using a charge depletion layer, the negatively charged vacancy complexes such as di-vacancy defects have been greatly removed during the growth process[30]. Hence, in our case, we suppose that the subsurface spin noise arises mostly from P1 centres, residual charged vacancy complexes and ^{13}C nuclear spins. Note that the two steps of charge manipulation ('pulling' and 'pushing') must be combined to enable coherence enhancement. No enhancement of the coherence time was observed if we only pushed the surface charge without first pulling the subsurface unpaired electrons onto the surface (Supplementary Fig. 4 and Supplementary Text 3). These findings suggest that the coherence enhancement arises not only from the local control of surface spins but also from the depletion of the subsurface paramagnetic defects. In addition, our 'pulling' step may also activate the electrons on the diamond surface into a certain surface state with high electron mobility, which might be attributed to the hydrated electrons[35] formed in the universally existing hydration layers on acid-cleaned diamond surfaces[36].

To further confirm that the suppressed noise comes from the unpaired electrons of the near-surface defects, we compared the DEER signals of a single NV before and after charge manipulation. As shown in Fig. 3b, when the coherence was enhanced, the difference between the DEER and spin-echo spectra was decreased. By fitting the normalized DEER spectra in a log–log plot (Methods)[34], we estimated that the density of unpaired electron spins on the diamond surface was reduced from $(3.10 \pm 0.38) \times 10^{15}\,\mathrm{m}^{-2}$ to $(0.3 \pm 0.05) \times 10^{15}\,\mathrm{m}^{-2}$ after the 'pull-and-push' strategy. We also found a noticeable change of the transition time in the power law in the normalized DEER spectra before and after T_2 enhancement,

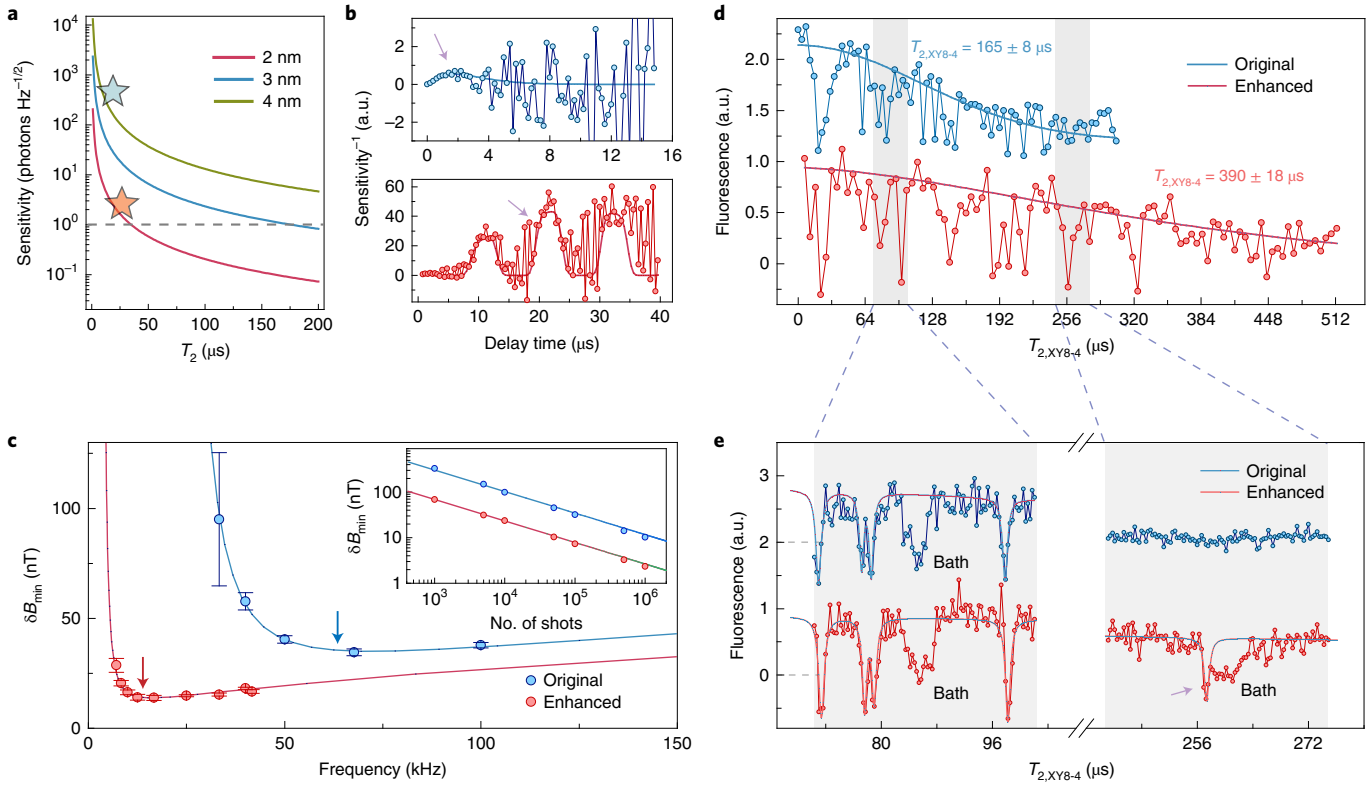

Fig. 4 | Demonstration of the improved sensitivity of the manipulated NV for quantum sensing. a, Calculated sensitivity for detecting external protons using shallow NVs with different depth and T_2 values. The typical sensitivity of shallow NV centres is marked by a blue star, while the result for the manipulated NV shown in Fig. 2b is marked by an orange star. The dashed grey line indicates 1 proton $Hz^{-1/2}$. **b**, Calculated sensitivity of the NV shown in Fig. 2b when detecting the incoherent magnetic signals such as external proton spins, with the original (upper) or enhanced (lower) coherence. The arrows indicate the calculated maximum sensitivity. The collapses of the sensitivity in the red curve result from the ^{13}C spin bath. The calculated sensitivity enhancement is ~80 fold. **c**, Normalized sensitivity by photon number per single shot for measurement of a harmonic AC magnetic field by a single shallow NV with a ~5-fold enhancement of T_2. The data show good consistency with theoretical predictions (solid lines). The sensitivity error bars produced during the measurements and data processing are indicated. The optimized sensitivity is marked by the arrows, clearly showing an enhancement of 2.5 fold. Besides, the lower bound of the detection bandwidth was also extended from ~33 kHz to less than 7 kHz. The inset demonstrates the photon shot noise-limited sensitivity, measured at the optimized frequency and fitted by $\delta B_{min} \propto N^{-0.47\pm0.01}$. **d**, Decoherence curves measured through XY8-4, showing a 2.4-fold lengthening of $T_{2,XY8-4}$. The two spectra are offset for clarity. **e**, Zoomed-in XY8-4 spectra in the shaded regions of **d**. The broad features showing decoherence into the mixing states are caused by the ^{13}C bath, while the isolated sharp peaks crossing over the zero points refer to single, coherently coupled nuclear spins. The red and blue curves are offset for clarity. Because of the coherence improvement, a single distant nuclear spin was resolved (arrow) around a delay time of ~257.4 μs (fifth order of spin bath). All the data in **c**–**e** were measured under 515.6 G.

suggesting a changed distribution of subsurface spins (Extended Data Fig. 3).

Since precisely mapping out the specific distributions of the spin bath in the vicinity of individual shallow NV is very challenging, a general protocol based on the spectral decomposition technique was utilized to analyse the decoherence noise spectra (Supplementary Text 4)[7]. Typical noise spectra before and after charge manipulation are shown in Fig. 3c (inset), where we fitted the data with a single Lorentz function and extracted the coupling strength between the spin bath and the NV centre. The peaks induced by the spin bath noise of ^{13}C are marked by dashed vertical lines, reflecting the periodic feature of Carr–Purcell–Meiboom–Gill (CPMG)'s filter function[37]. It is clear that the magnetic noise ranging from ~10 kHz to 300 kHz is considerably suppressed after the charge manipulation.

From the dependence of the coupling strength on the original T_2 (Supplementary Text 4), the sources of the noise can be analysed by using the simple model shown in Fig. 3a. The coupling strength versus original T_2 of different NVs is plotted in Fig. 3c. The coupling strength both before (Δ_i) and after (Δ_f) coherence enhancement show a notable dependence on T_2. Considering the positive relation between T_2 and NV depth (Extended Data Fig. 2), such a dependence is consistent with the ~$1/d^2$ relation of coupling strength between NV and the surface noise[6]. Remarkably, for NVs with an original T_2 time longer than 10 μs (corresponding to a depth of ~5 nm; Fig. 3c, dashed line), the differential coupling strength ($\Delta_i - \Delta_f$) only shows a weak dependence on T_2. Such a result can be understood by considering that the spin noise at the subsurface was roughly homogeneous in space around the relatively deep NV centres (Fig. 3a, dark red arrow). The decreased coupling strength in the noise spectra is about 0.2–0.3 MHz (Fig. 3c), approximately half of the residual bulk noise strength reported for boron-doped samples[30].

In contrast, a very large differential coupling strength was observed for NVs with poor coherence time (<10 μs) (Fig. 3c). This results from the fact that such NVs are in closer proximity to the diamond surface (Fig. 3a, light red arrow) and thus suffer from stronger coupling with the surface spins in their vicinity, which were induced during NV growth and then suppressed through our 'pull-and-push' method. These findings clearly indicate a transition of the dominant decoherence sources from subsurface spins to surface spins as the depth of the NV centre is decreased (Fig. 3c, vertical dashed line).

It is worth noting that, even if the T_2 time of shallow NVs was enhanced by more than two fold on average after suppressing the electron spin noise, we did not find changes of T_2^* beyond the fitting errors in the free-induction decay spectra (Supplementary Fig. 5). We excluded the inhomogeneous broadening caused by the slightly drifted local electric field from the tip, since we only found a variation of ~10% for T_2^* under large bias when the tip was located hundreds of nanometres horizontally away from the NV centre (Supplementary Fig. 5). Instead, we attributed it to the unavoidable complex charge dynamics near the diamond surface under the illumination by the 532 nm lasers during the measurements. Typically, the charge dynamics leads to low-frequency spin noise ranging from several tens to hundreds of kilohertz, which limits T_2^* (Supplementary Text 3).

Figure 4a shows the calculated sensitivity of shallow NVs with different depth and T_2 values for sensing external protons (Supplementary Text 5). The result for the enhanced NV shown in Fig. 2b is marked by an orange star, demonstrating an upper bound for the sensitivity close to just a single external proton. It is expected that the application of more complex pulse sequences such as the dynamical decoupling sequences[4,13], correlation[38], weak measurements[39,40] and advanced readout[14,29,41] techniques generally used in nanoscale nuclear magnetic resonance (NMR) may further push the sensitivity to $(92\,\mathrm{nT})^2\,\mathrm{Hz}^{-1/2}$ to $(172\,\mathrm{nT})^2\,\mathrm{Hz}^{-1/2}$, corresponding to a sub-proton sensitivity of 0.12–0.42 protons $\mathrm{Hz}^{-1/2}$ for an NV depth of ~2.2 nm (Supplementary Text 5). Figure 4b shows the calculated sensitivity enhancement of a manipulated NV for detecting subtle incoherent magnetic signals, which naturally exist in nanoscale spin structures such as proton clusters[3,4,13,14] and single proteins[29]. In such a case, the minimum detectable magnetic field scales with $C\,(T_2)^{-1}\,T_2^{-3/2}$. According to the fitted curve (solid lines), the sensitivity enhancement is defined by the ratio between the highest sensitivities in the enhanced and original conditions as obtained from the fitted curves (marked by arrows), yielding an 80-fold enhancement for a 20-fold lengthening of T_2 (Supplementary Text 6)[10,29]. We emphasize that this theoretical prediction is based on tiny phase accumulations. Actually, proton detection requires a signal contrast beyond the background fluctuation, which may reduce the sensitivity enhancement measured in experiments (Extended Data Fig. 4 and Methods). For sensing an external harmonic AC magnetic field, the minimum detectable magnetic field δB_{min} scales with $C\,(T_2)^{-1}\,T_2^{-1/2}$ (Supplementary Fig. 6 and Supplementary Text 7)[2,25]. In Fig. 4c, using the spin echo sequence, a 2.5-fold sensitivity enhancement was obtained for a 5-fold lengthening of T_2. Accordingly, when applying the same number of shots for readout, the minimum detectable magnetic field for the prolonged T_2 was 4.4 times smaller (Fig. 4c, inset). At the same time, the lower bound of the detection bandwidth was also extended from ~33 kHz to less than 7 kHz.

To further confirm that the enhanced sensitivity is important for detecting more subtle magnetic fields, we applied an XY8-4 sequence (a similar pulse sequence with CPMG except the alternative rotating axis of NV during the π-pulses) and tried to measure weakly coupled nuclear spins around the NV centre[42]. As shown in Fig. 4d, after suppressing the bath noise from electron spins through the charge manipulation method, we obtained an enhanced coherence under the dynamical decoupling sequence (Fig. 4d, red curve). Figure 4e shows zooms at the second- and fifth-order resonances of the ^{13}C bath. A longer interrogation time for accumulating the external magnetic field gives higher spectral resolution in the dynamical decoupling spectra[42]. In the fifth-order region of the red spectra, a sharp peak (arrow) was isolated from the broad decoherence feature caused by the ^{13}C bath, while no clear feature was found in the blue spectra measured before charge manipulation. Since the curves measured with a last microwave pulse of π/2 or 3π/2 during a single cycle show a distinct cross-over feature at this peak (Supplementary Fig. 7), we determine this to corresponding to a single coherently coupled ^{13}C nuclear spin with a coupling strength of $A_{||} \approx 15.18$ kHz with the NV centre. This sensitivity is comparable to the results ($A_{||}$ of 1–10 kHz) reported when using deep NV centres in bulk diamond[42].

In this work, we developed a new method for substantially enhancing the coherence of single shallow NVs, which improves prior limitations on the application of solid-state qubits for quantum sensing. In particular, such coherence boosting of extremely shallow (<5 nm) NVs may open up a new possibility for quantum sensing to detect ultra-weak signals such as those from single-proton nuclear spins or even sub-proton nuclear spins (Extended Data Fig. 4), which is a longstanding goal in micro- and nanoscale magnetometry. It is expected that well-controlled surface treatments should further improve or optimize our 'pull-and-push' method. More generally, our method provides a powerful and universal toolkit for enhancing the coherence of other kinds of near/on-surface solid-state qubits[43] such as colour centres in 2D materials[44], SiV in diamond[45] and SiV or di-vacancies in SiC[12,46]. Besides, this method is also suitable for enhancing the coherence of non-fluorescent defects in diamond, such as P1 centres, to make them excellent auxiliary qubits for high-performance quantum information technology[47].

Online content

Any methods, additional references, Nature Research reporting summaries, source data, extended data, supplementary information, acknowledgements, peer review information; details of author contributions and competing interests; and statements of data and code availability are available at https://doi.org/10.1038/s41567-022-01719-4.

Received: 8 August 2021; Accepted: 13 July 2022;
Published online: 25 August 2022

References

1. Balasubramanian, G. et al. Nanoscale imaging magnetometry with diamond spins under ambient conditions. *Nature* **455**, 648–651 (2008).
2. Maze, J. R. et al. Nanoscale magnetic sensing with an individual electronic spin in diamond. *Nature* **455**, 644–647 (2008).
3. Mamin, H. J. et al. Nanoscale nuclear magnetic resonance with a nitrogen-vacancy spin sensor. *Science* **339**, 557–560 (2013).
4. Staudacher, T. et al. Nuclear magnetic resonance spectroscopy on a (5-nanometer)^3 sample volume. *Science* **339**, 561–563 (2013).
5. Shi, F. Z. et al. Single-protein spin resonance spectroscopy under ambient conditions. *Science* **347**, 1135–1138 (2015).
6. Rosskopf, T. et al. Investigation of surface magnetic noise by shallow spins in diamond. *Phys. Rev. Lett.* **112**, 147602 (2014).
7. Romach, Y. et al. Spectroscopy of surface-induced noise using shallow spins in diamond. *Phys. Rev. Lett.* **114**, 017601 (2015).
8. Myers, B. A., Ariyaratne, A. & Jayich, A. C. B. Double-quantum spin-relaxation limits to coherence of near-surface nitrogen-vacancy centers. *Phys. Rev. Lett.* **118**, 197201 (2017).
9. de Lange, G., Wang, Z. H., Riste, D., Dobrovitski, V. V. & Hanson, R. Universal dynamical decoupling of a single solid-state spin from a spin bath. *Science* **330**, 60–63 (2010).
10. Bluvstein, D., Zhang, Z. R., McLellan, C. A., Williams, N. R. & Jayich, A. C. B. Extending the quantum coherence of a near-surface qubit by coherently driving the paramagnetic surface environment. *Phys. Rev. Lett.* **123**, 146804 (2019).
11. Li, R. et al. Nanoscale electrometry based on a magnetic-field-resistant spin sensor. *Phys. Rev. Lett.* **124**, 247701 (2020).
12. Miao, K. C. et al. Universal coherence protection in a solid-state spin qubit. *Science* **369**, 1493–1497 (2020).
13. Schmitt, S. et al. Submillihertz magnetic spectroscopy performed with a nanoscale quantum sensor. *Science* **356**, 832–837 (2017).
14. Aslam, N. et al. Nanoscale nuclear magnetic resonance with chemical resolution. *Science* **357**, 67–71 (2017).
15. Abobeih, M. H. et al. Atomic-scale imaging of a 27-nuclear-spin cluster using a quantum sensor. *Nature* **576**, 411–415 (2019).
16. Gross, I. et al. Real-space imaging of non-collinear antiferromagnetic order with a single-spin magnetometer. *Nature* **549**, 252–256 (2017).
17. Thiel, L. et al. Probing magnetism in 2D materials at the nanoscale with single-spin microscopy. *Science* **364**, 973–976 (2019).

18. Ku, M. J. H. et al. Imaging viscous flow of the Dirac fluid in graphene. *Nature* **583**, 537–541 (2020).
19. Dolde, F. et al. Electric-field sensing using single diamond spins. *Nat. Phys.* **7**, 459–463 (2011).
20. Bian, K. et al. Nanoscale electric-field imaging based on a quantum sensor and its charge-state control under ambient condition. *Nat. Commun.* **12**, 2457 (2021).
21. Kucsko, G. et al. Nanometre-scale thermometry in a living cell. *Nature* **500**, 54–58 (2013).
22. Neumann, P. et al. High-precision nanoscale temperature sensing using single defects in diamond. *Nano Lett.* **13**, 2738–2742 (2013).
23. Wu, Y. Z., Jelezko, F., Plenio, M. B. & Weil, T. Diamond quantum devices in biology. *Angew. Chem. Int. Ed.* **55**, 6586–6598 (2016).
24. Le Sage, D. et al. Optical magnetic imaging of living cells. *Nature* **496**, 486–489 (2013).
25. Taylor, J. M. et al. High-sensitivity diamond magnetometer with nanoscale resolution. *Nat. Phys.* **4**, 810–816 (2008).
26. Degen, C. L., Reinhard, F. & Cappellaro, P. Quantum sensing. *Rev. Mod. Phys.* **89**, 035002 (2017).
27. Barry, J. F. et al. Sensitivity optimization for NV-diamond magnetometry. *Rev. Mod. Phys.* **92**, 015004 (2020).
28. Deak, P., Aradi, B., Kaviani, M., Frauenheim, T. & Gali, A. Formation of NV centers in diamond: a theoretical study based on calculated transitions and migration of nitrogen and vacancy related defects. *Phys. Rev. B* **89**, 079905 (2014).
29. Lovchinsky, I. et al. Nuclear magnetic resonance detection and spectroscopy of single proteins using quantum logic. *Science* **351**, 836–841 (2016).
30. de Oliveira, F. F. et al. Tailoring spin defects in diamond by lattice charging. *Nat. Commun.* **8**, 15409 (2017).
31. Sangtawesin, S. et al. Origins of diamond surface noise probed by correlating single-spin measurements with surface spectroscopy. *Phys. Rev. X.* **9**, 031052 (2019).
32. Giessibl, F. J. Advances in atomic force microscopy. *Rev. Mod. Phys.* **75**, 949–983 (2003).
33. Giessibl, F. J. The qPlus sensor, a powerful core for the atomic force microscope. *Rev. Sci. Instrum.* **90**, 011101 (2019).
34. Dwyer, B. L. et al. Probing spin dynamics on diamond surfaces using a single quantum sensor. Preprint at https://arxiv.org/abs/2103.12757 (2021).
35. Hammer, N. I. et al. How do small water clusters bind an excess electron? *Science* **306**, 675–679 (2004).
36. Hauf, M. V. et al. Chemical control of the charge state of nitrogen-vacancy centers in diamond. *Phys. Rev. B* **83**, 081304 (2011).
37. Zhao, N. et al. Sensing single remote nuclear spins. *Nat. Nanotechnol.* **7**, 657–662 (2012).
38. Staudacher, T. et al. Probing molecular dynamics at the nanoscale via an individual paramagnetic centre. *Nat. Commun.* **6**, 8527 (2015).
39. Pfender, M. et al. High-resolution spectroscopy of single nuclear spins via sequential weak measurements. *Nat. Commun.* **10**, 594 (2019).
40. Cujia, K. S., Boss, J. M., Herb, K., Zopes, J. & Degen, C. L. Tracking the precession of single nuclear spins by weak measurements. *Nature* **571**, 230–233 (2019).
41. Shields, B. J., Unterreithmeier, Q. P., de Leon, N. P., Park, H. & Lukin, M. D. Efficient readout of a single spin state in diamond via spin-to-charge conversion. *Phys. Rev. Lett.* **114**, 136402 (2015).
42. Taminiau, T. H. et al. Detection and control of individual nuclear spins using a weakly coupled electron spin. *Phys. Rev. Lett.* **109**, 137602 (2012).
43. Wolfowicz, G. et al. Quantum guidelines for solid-state spin defects. *Nat. Rev. Mater.* **6**, 906–925 (2021).
44. Gottscholl, A. et al. Initialization and read-out of intrinsic spin defects in a van der Waals crystal at room temperature. *Nat. Mater.* **19**, 540–545 (2020).
45. Evans, R. E. et al. Photon-mediated interactions between quantum emitters in a diamond nanocavity. *Science* **362**, 662–665 (2018).
46. Widmann, M. et al. Coherent control of single spins in silicon carbide at room temperature. *Nat. Mater.* **14**, 164–168 (2015).
47. Degen, M. J. et al. Entanglement of dark electron-nuclear spin defects in diamond. *Nat. Commun.* **12**, 3470 (2021).

Methods

Experimental setup. All the data in this work were recorded in our home-built scanning probe microscope (SPM) system, which was specially designed for achieving excellent compatibility with NV centre technology. The SPM part includes a compact Pan-type scanner head[48], integrated with vector magnets and high-frequency transmission cables. An oil-immersed objective (numerical aperture 1.3) was used for photon collection, and the focus spot is driven by a commercial piezo-driven scanner (Physik Instrumente). We chose a qPlus sensor equipped with a tungsten tip (25 μm diameter) for AFM measurements[33]. The tungsten tip was first electrochemically etched in NaOH solution and subsequently cleaned and sharpened by using an FIB with a small beam current (typically <80 pA and 30 kV). The bias voltage was supplied by the AO output of an NI-DAQ (National Instrument) and amplified through a commercial piezo driver (−450 V to +450 V, CoreMorrow). The bias was applied on the tip, while the ground reference was on the microwave waveguide and the shielding box of the SPM scanner.

Single NV centres were addressed individually by using our home-built confocal imaging system. The spin state of NV^- was initialized by using a 532 nm laser and read out by collecting the emitted photons in an avalanche photodiode (Excelitas). The 532 nm laser was chopped by using an acoustic-optic modulator (Gooch & Housego) crystal in double-pass mode and subsequently shaped by a single-mode fibre. The microwaves were generated by a signal generator (N5181B, Keysight), split by a 90° hybrid, chopped by switchers, amplified by a power amplifier and finally fed through the microwave waveguide used for flipping the electron spin of NV^-. The synchronization of the laser pulse, microwave pulse and counter timing was achieved by using a multi-channel digital pulse generator (PBESR-500, Spincore). All the spin echo and dynamical decoupling measurements were acquired by the subtraction of two measured decoherence spectra, with the last microwave pulses being set as $\pi/2$ and $3\pi/2$ individually. For NMR measurement of external protons, we replaced the multi-channel digital pulse generator with an arbitrary wave generator (DN2-662.04, SPECTRUM) combined with an external IQ modulator (MMIQ-0218L, Marki).

NV creation. The diamonds used in this work are electronic-grade single-crystal chips purchased from Element Six, with intrinsic nitrogen concentration below 5 ppb. The chips were milled into membranes with thickness of 20–30 μm by laser cutting at DDK Inc. The diamond membranes were then prepared as described in ref. [30]. First, an epitaxial boron-doped layer of diamond is grown by microwave-assisted chemical vapour deposition. The thickness of such a layer is ~9 nm with a boron concentration above $10^{20}\,cm^{-2}$. Next, the diamond with the boron-doped layer was implanted with 5 keV ^{15}N ions at a tilt angle of 3° to the normal direction of the diamond surface with an average dose of $5\times10^9\,cm^{-2}$. A subsequent high-temperature anneal at 950 °C for 2 h led to diffusion of carbon vacancies, which ultimately combined with ^{15}N donors. The sample was then cleaned by boiling in tri-acid solution. Finally, an ion etching process using O_2 was applied to remove a ~15 nm thickness of diamond in an inductively coupled plasma reactive ion etching system, which results in the shallow NVs with depth of ~5 nm.

Charge state control. A detailed description of the recipe used for precise and high-fidelity charge state control can be found in previous work[20]. Because of the scattering of the 532 nm laser with power of ~300 μW, the tip can be resolved in the confocal image and brought close to a selected NV centre. Then, we focused the laser on this NV and scanned the tip with a large positive bias (typically larger than +50 V) around it within a region of 1–2 μm^2, leading to polarization of the surface by pulling the unpaired electrons from the subsurface paramagnetic defects onto the surface (Extended Data Fig. 5). In this case, when the tip bias and parking time per pixel are fixed, the area of polarized surface is mainly dependent on the power of the excitation laser. Considering the typical size of our laser focus and the power used during the 'pulling' step, we estimate a polarized area of ~265 × 265 nm^2 for a laser power of ~300 μW and a tip bias of +50 V (Extended Data Fig. 5). After the scanning, the tip was grounded or retracted, while the surface polarization remained due to trapping of the surface electrons in deep defect levels. The induced built-in electric field brought the bright state (NV^-) into the dark state (NV^+), which was intrinsically stable at room temperature. The charge state will recover to NV^- either through the tip-induced band bending effect or direct depolarization of the surface under a large negative voltage (typically larger than −60 V). It is noteworthy to state that, even under large bias voltages and high-power laser excitation during the surface polarization, no changes in AFM tomography were observed.

Suitable tip position for the 'pushing' step. It is worth noting that, during the 'pushing' step, the tip with large negative bias should not be brought into proximity with the NV centre. In this case, the electric field of the tip would lead to upward band bending and turn the NV^- to the NV^+ state (Extended Data Fig. 1a), which is not applicable for spin echo measurements. When the laser power is large enough, the surface can even become depolarized at the large negative bias due to ionization of surface charges, thus recovering the NV^- state[20]. In the current case, we only used a low-power laser during the 'pushing' step, to avoid irreversible depolarization of the polarized surface (Supplementary Fig. 2b), thus the ionization of the surface charges is suppressed and only the tip-induced band bending effect dominates (Extended Data Fig. 1b).

To provide more details on the tip position during the 'pushing' step, we performed spin echo mapping (Extended Data Fig. 1). We first selected a NV with an original T_2 of 22 μs and turned it into the NV^+ state through the 'pulling' step. Then, we fixed the delay time of the spin echo at 14 μs, scanned the tip with a negative bias and monitored the spin echo signal continuously. Extended Data Fig. 1c and 1d demonstrate the spin-echo signal mapping under tip bias of −100 and −150 V, respectively. The NV's position is marked by a white disc whose position and size are determined by the quenching effect of the metal tip (Supplementary Fig. 3). An overall decay of the spin echo signal along the scanning direction (dashed arrow) was caused by thermal drift during the long-term data acquisition (~6 h per image).

In the spin echo mapping, a larger signal at fixed delay time indicates a higher spin contrast and thus longer T_2. From the spin echo mapping, we can identify the 'hot' regions highlighted by the dashed curves, corresponding to the tip position for achieving the optimal T_2 enhancement during the 'pushing' step. In Extended Data Fig. 1c, the 'hot' region is located roughly 300–700 nm away from the NV centre. The existence of the 'hot' region arises from two competing factors. On the one hand, a small tip–NV distance will cause the upward band bending effect and make the charge state of NV^- unstable (Extended Data Fig. 1a,b). On the other hand, when the tip is too far away from the NV, the field strength is insufficient to push the surface electrons efficiently. This is also confirmed by the spatially dependent spin echo measurements with fitted T_2 in Extended Data Fig. 1e. The higher tip bias induces a 'hotter' and 'wider' region for optimal T_2 enhancement during the 'pushing' step (Extended Data Fig. 1d). The shape of the 'hot' region seems irregular and asymmetric, which may be caused by the asymmetric shape of the tip, the random distribution of the surface charge and the re-organization of the surface charge during the spin echo mapping.

Depth calibration of shallow NVs through DEER spectra. The depth of the NVs can be estimated from DEER spectra by using the model of configurational averaged surface spins[34]. In the DEER measurement, an extra microwave π-pulse is applied at the middle of the spin echo sequence, aiming to flip the polarization direction of paramagnetic electron spins such as P1 centres, charged vacancies and surface electron spins surrounding the NV centre (Extended Data Fig. 2a). In this way, the tiny magnetic fields from the flipped electron spins can be sensed by the NV during the interrogation time τ, while the background from the non-flipped ones is cancelled. Thus, the DEER spectra $D(\tau)$ (Extended Data Fig. 2b, blue curve) shows additional decoherence compared with the spin echo measurement $C(\tau)$ (Extended Data Fig. 2b, red curve). To cancel out the oscillations in $D(\tau)$ and $C(\tau)$ caused by the residual spin noise from ^{13}C or misalignment of the bias magnetic field, we obtained normalized DEER spectra as $S(\tau)=D(\tau)/C(\tau)$ (Extended Data Fig. 2c).

In the case of the diluted surface spins, the normalized DEER spectra show a stretched exponential decay with different exponents n ranging from 2/3 to 2. When τ is small, all the surrounding electron spins are distant from NV and can be regarded as a quasi-static bath, leading to a DEER decay with Gaussian shape, that is, $n=2$. However, at very large τ, the NV is strongly coupled to a few surface spins that hop around occasionally during the repetitions of the measurements, leading to $n=2/3$ (ref. [34]). To clearly show the exponent of the power law, we applied the logarithm of $S(\tau)$, as in ref. [34]. Typically, DEER spectra can be described by a single power law:

$$S(\tau)=\exp\left(-\left(\frac{\tau}{\tau_{DEER}}\right)^n\right), \tag{1}$$

where $1/\tau_{DEER}$ is the decay rate of the DEER spectra. We can then define

$$g(\tau)=\log_{10}\ln\left(\frac{1}{S(\tau)}\right). \tag{2}$$

Extended Data Fig. 2d shows $g(\tau)$ on a log–log plot, where the exponent of the power law n is reflected by the slope of the curve. A depth-dependent transition time should be found in $g(\tau)$, which can be used for NV depth calibration with precision comparable to NMR measurements[34]. We fit $S(\tau)$ by the following function, with the depth d and the surface spin density σ as the fitting parameters:

$$S(\tau)=\exp\left\{\sigma\int_0^{2\pi}d\alpha\int_0^{\infty}rdr\times\left(\cos\frac{\mu_0\gamma_e^2\hbar\tau(2r^2\cos^2\alpha-r^2-2\sqrt{2}rd\cos\alpha)}{8\pi(r^2+d^2)^{5/2}}-1\right)\right\}, \tag{3}$$

where r is the relative distance of an electron noise to the NV and α is the polar angle. The fitted depths of seven measured NVs are summarized in Extended Data Fig. 2e, where a positive relation between the depth and the spin echo time is clearly seen. It can be seen that the NVs with $T_2<10$ μs are located within 5 nm of the surface. The NV with T_2 of 1.5 μs shows a depth of only 2.5 nm, which suggests that the depth of the NV ($T_2=1.3$ μs) shown in Fig. 2b is ~2.2 nm.

We note that the model described above only considers the contributions from the on-surface electron spins to the DEER measurements. The contribution from the subsurface spins may lead to discrepancies between the estimated and real depth. However, this model should still be valid for extremely shallow NVs with depth <5 nm, where the contribution from on-surface spins to DEER measurements is dominant (Fig. 3c). For relatively deep NVs, that is, >5 nm, the contribution from the subsurface electron spins to DEER signals is considerable, leading to a discrepancy of ~1 nm in the depth estimation.

Measuring the sensitivity enhancement for proton detection. The theoretical calculation (Fig. 4a,b) of the sensing magnetic field variance in Supplementary Texts 5 and 6 is based on the approximation of the tiny phase accumulation of the NV centre during the measurements. Therefore, the resulting sensitivity does not depend on the detected signal strength but rather scales as $T_2^{-3/2}$, leading to a simple and clean standard for evaluating the important role of T_2 in quantum sensing of weak magnetic signals such as proton spins.

In experiments, the spin echo is practically not applicable for proton detection due to its limited spectral resolution in picking up the precession frequency of protons. In contrast, we need to apply a large number of π-pulses to obtain enough phase accumulation and signal contrast, which is described by[49]

$$\begin{aligned} S_{\mathrm{DD}}\left(B_{\mathrm{rms}}^2\right) &= C\left(n\tau\right)\left(1-\langle\cos\Delta\phi\rangle\right) \\ &= C(n\tau)(1-\exp(-\tfrac{2}{\pi^2}\gamma_e^2 B_{\mathrm{rms}}^2 K(n\tau))), \end{aligned} \tag{4}$$

where B_{rms}^2 is the magnetic variance from the ensemble of protons, $\tau = f/2$ equals half the precession period of protons, $\langle\cos\Delta\phi\rangle$ is the averaged normalized signal of different measurement cycles, γ_e is the gyromagnetic ratio of the NV centre, $C(n\tau)$ represents the spin contrast of the NV at the π–π delay time of τ in a dynamical decoupling sequence such as XY8-k, $n = 8k$ is the total number of π pulses and $K(n\tau)$ is a function determined by the filter function of XY8-k and the finite coherence time of the protons.

According to the definition of sensitivity, we obtained the minimum detectable magnetic field variance as equal to the sensitivity obtained at the specific N, where N is the number of shots for readout:

$$\delta B_{\mathrm{rms}}^2 = \sigma_S^N/\max\left(\frac{\partial S_{\mathrm{DD}}}{\partial B_{\mathrm{rms}}^2}\right) = \sigma_S^N/\left(\frac{2}{\pi^2}\gamma_e^2 \mathrm{K}(n\tau)\mathrm{C}(n\tau)\,\langle\cos\Delta\phi\rangle\right), \tag{5}$$

where σ_S^N scaled with $(n\tau)^{1/2}$ is the photon shot noise-limited uncertainty after N number of XY8-k measurements. The maximum of the derivative of S_{DD} is difficult to obtain in experiment since it is difficult to control the number of protons in ambient conditions and usually an ensemble of protons contribute to the signals (Extended Data Fig. 4a). Instead, we can only evaluate the sensitivity at specific B_{rms} through equation (5).

When B_{rms} is small (such as ~100 nT), the maximum signal contrast requires $n\tau$ to approach $T_{2,\mathrm{XY8}\text{-}k}$, which can be realized by increasing the π number n. Generally, a longer $T_{2,\mathrm{echo}}$ leads to longer $T_{2,\mathrm{XY8}\text{-}k}$ and larger n, which would enhance the sensitivity for proton detection within the region of small signal contrast according to equation (5) (Extended Data Fig. 4b, highlighted region and blue curve). In actual experiments, the signal contrast should be larger than the background fluctuation of the fluorescence. To obtain a convincing proton signal from XY8-k, we need to apply a large number of π pulses and achieve sufficient signal contrast (typically larger than 30% in our case), which might decrease the sensitivity (Extended Data Fig. 4b, red curve). Therefore, the theoretical estimation of the sensitivity shown in Fig. 4b demonstrates the upper limit for sensing subtle signals using a sensor with a coherence time of T_2.

In the following, we demonstrate the experimental enhancement of the sensitivity for detecting proton spins. NVs showing large T_2 enhancement (~20 fold) usually have very poor coherence ($T_2 \approx 1$ μs, depth ~2 nm) (Extended Data Fig. 4c), making it difficult to detect external protons. In the original condition, we can only apply 16 π-pulses for dynamical decoupling (that is, XY8-2 for the blue curve in Extended Data Fig. 4d, while the coherence is totally collapsed with more π pulses) and obtain no proton signals. However, after using the 'pull-and-push' method described in the main text, T_2 was enhanced to 18 μs and a clear dip appears at around 387 ns when applying XY8-12, consistent with the precession frequency of protons under 303 G. Based on equations (4) and (5), the minimum detectable magnetic variance after an integration time of 4,800 s in Extended Data Fig. 4d is $\delta B_{\mathrm{rms}}^2 = (129.5\,\mathrm{nT})^2$, corresponding to ~0.18 proton spins, considering the estimated depth of 2.1 nm for this NV.

Unfortunately, it is impossible to quantitatively calculate the sensitivity enhancement, since the proton signal is not detectable before the coherence enhancement. Although the exact value of the sensitivity enhancement cannot be given in experiments, we demonstrated that, when using our method, a quantum sensor with extremely poor coherence was truly improved to achieve high sensitivity for sensing subtle magnetic fields from external nuclear spins such as protons.

Data availability

Source data that support the findings of this study are available with this paper. All other data that support the plots within this paper are available from the corresponding authors upon reasonable request. Source data are provided with this paper.

Code availability

The custom codes for fitting the data are available from the corresponding authors upon reasonable request.

References

48. Pan, S. H., Hudson, E. W. & Davis, J. C. He-3 refrigerator based very low temperature scanning tunneling microscope. *Rev. Sci. Instrum.* **70**, 1459–1463 (1999).
49. Pham, L. M. et al. NMR technique for determining the depth of shallow nitrogen-vacancy centers in diamond. *Phys. Rev. B* **93**, 045425 (2016).

Acknowledgements

We thank F. Giessibl for his valuable help on qPlus-based AFM under ambient condition. This work was supported by the National Key R&D Program under grant nos. 2021YFA1400500 and 2017YFA0205003, the National Natural Science Foundation of China under grant nos. 11888101 and 21725302 and the Strategic Priority Research Program of the Chinese Academy of Sciences under grant no. XDB28000000. Y.S. and S.Y. were supported by Hong Kong RGC (GRF/14304618). R.S., A.D. and J.W. were supported by the ERC grant SMeL and the VW Foundation.

Author contributions

Y.J. and S.Y. designed and supervised the project. K.B. constructed the experimental setup. R.S. and A.D. grew the diamond chips and fabricated the shallow NVs. W.Z. and K.B. performed the experiments and data acquisition. W.Z., K.B., X.C., Y.S., S.C., J.W., S.Y. and Y.J. performed the data analysis and interpretation. K.B., S.Y. and Y.J. wrote the article, with input from all other authors. All the authors commented on the final article.

Competing interests

The authors declare no competing interests.

Additional information

Extended data is available for this paper at https://doi.org/10.1038/s41567-022-01719-4.

Supplementary information The online version contains supplementary material available at https://doi.org/10.1038/s41567-022-01719-4.

Correspondence and requests for materials should be addressed to Ke Bian, Sen Yang or Ying Jiang.

Peer review information *Nature Physics* thanks Helena Knowles and the other, anonymous, reviewer(s) for their contribution to the peer review of this work.

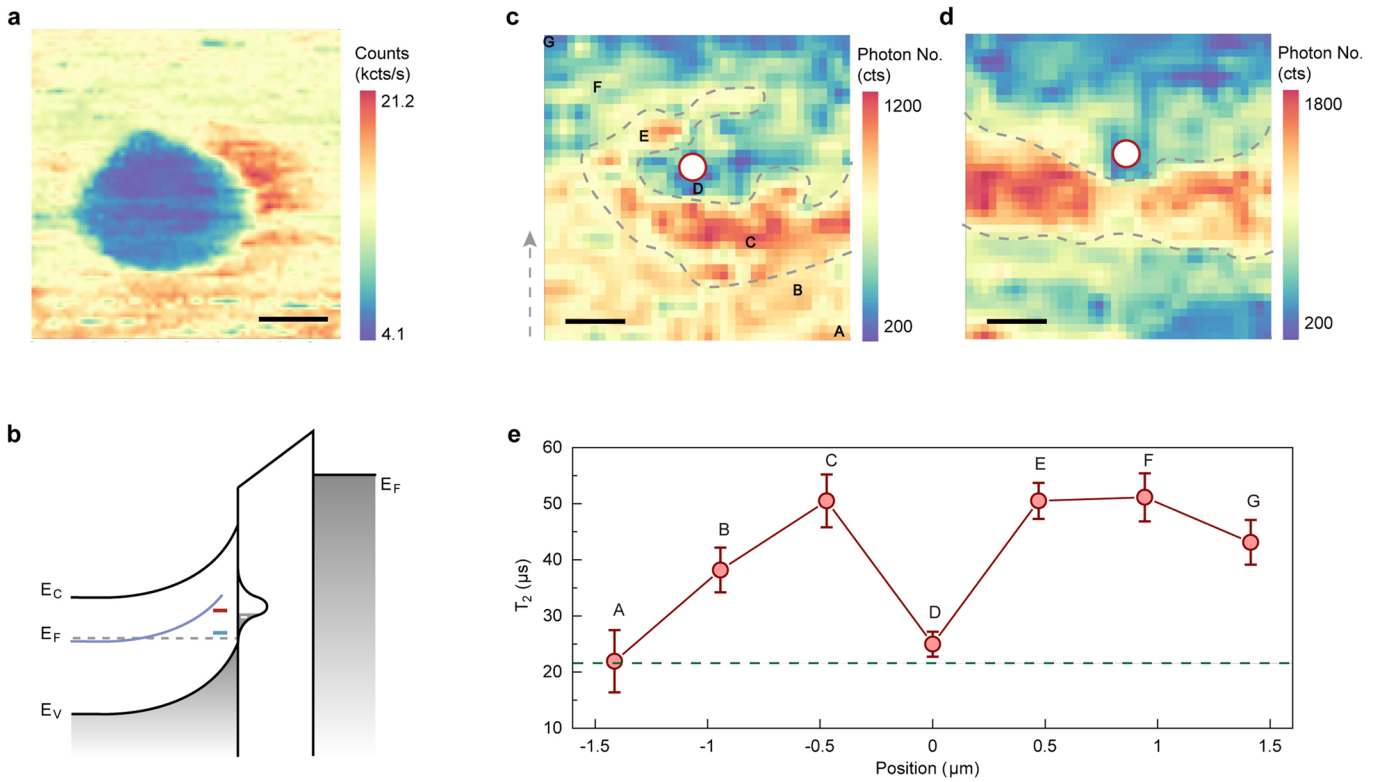

Extended Data Fig. 1 | Suitable tip position for T_2 enhancement in 'pushing' step. a, The confocal mapping when a negatively biased tip is scanned over a single shallow NV centre. The dark disk-like feature corresponds to NV^+ state, caused by the strong tip-induced upward band bending effect. Scale bar: 500 nm. Laser power: 30 μW. Tip bias: −220 V. **b**, Schematic diagram showing the tip-induced band bending effect. When the tip is laterally close to NV within 300 nm, the large upward band bending effect induced by the negatively biased tip leads to NV^+ state. The charge transition levels of NV^+/NV^0 and NV^0/NV^- are denoted by the short blue and red lines, respectively. The charge transition level of paramagnetic spins is denoted by the purple line. E_F is the Fermi level, E_C and E_V denote the edges of the conduction and valance bands, respectively. **c**,**d**, Spin-echo mapping of one NV centre in the 'pushing' step under the tip bias of −100 V and −150 V, respectively, by fixing the delay time of spin-echo measurements. The images were expanded from 20 × 20 pixels to 40 × 40 pixels through the interpolation. The white disc denotes the position of NV. A grey arrow denotes the scanning direction, along which an overall decay of spin-echo signal was observed due to the thermal drift during the 6-hours imaging. The 'hot' regions demonstrating the longer T_2 time are highlighted by the dashed curves. Scale bar: 400 nm. **e**, The T_2 measurements at different positions in **c**. At every position denoted by the alphabets in **c**, we applied spin-echo measurements at full time range and fitted the T_2. The dashed horizontal line denotes the original T_2. The variation of T_2 in **e** indicates the suitable tip position for enhancing the T_2 under the 'pushing' step.

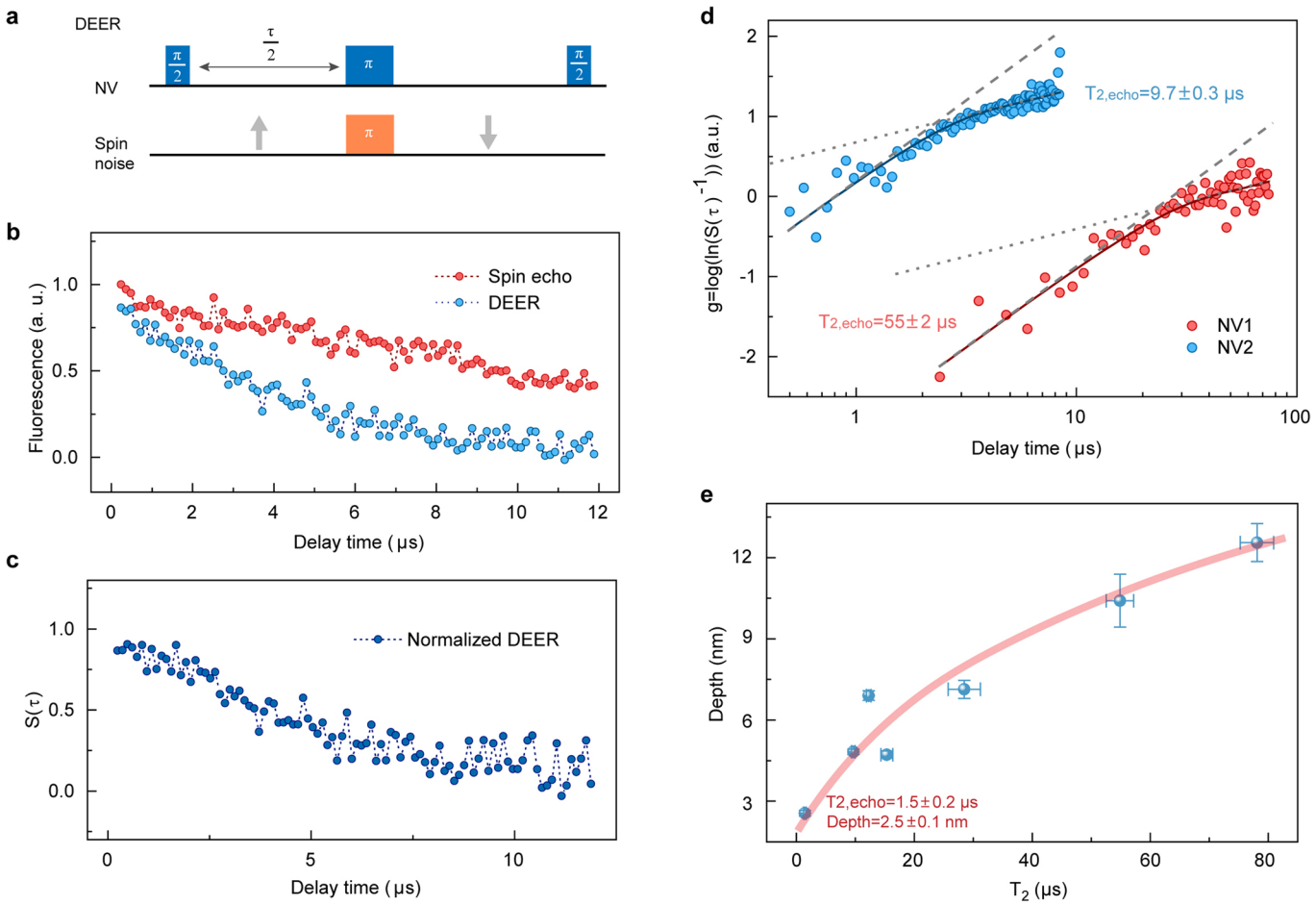

Extended Data Fig. 2 | DEER spectra for depth calibration of shallow NVs. a, Schematics showing the principle of DEER measurement. An extra π-pulse is applied at the middle of the spin-echo sequence, flipping the surrounding electron spins. Thus, the magnetic field from electron spins is sensed by the NV centre. **b**, Typical results of DEER spectra and spin-echo of a single shallow NV. Additional decoherence caused by the electron spins obviously appears in the DEER. **c**, Normalized DEER spectra for eliminating unwanted oscillations and peaks caused by the ^{13}C residual spins or misalignment of biased magnetic field. **d**, Two typical normalized DEER spectra demonstrated in log-log plot of two shallow NV centres. The transition time is clearly observed, which reflects the depth of the NV centres. The dashed and dotted lines represent the powers of 2 and 2/3, respectively. **e**, The graph summarizing seven measured NV centres, which shows a positive relation between T_2 and the depth. The red curve is used for guiding the eyes.

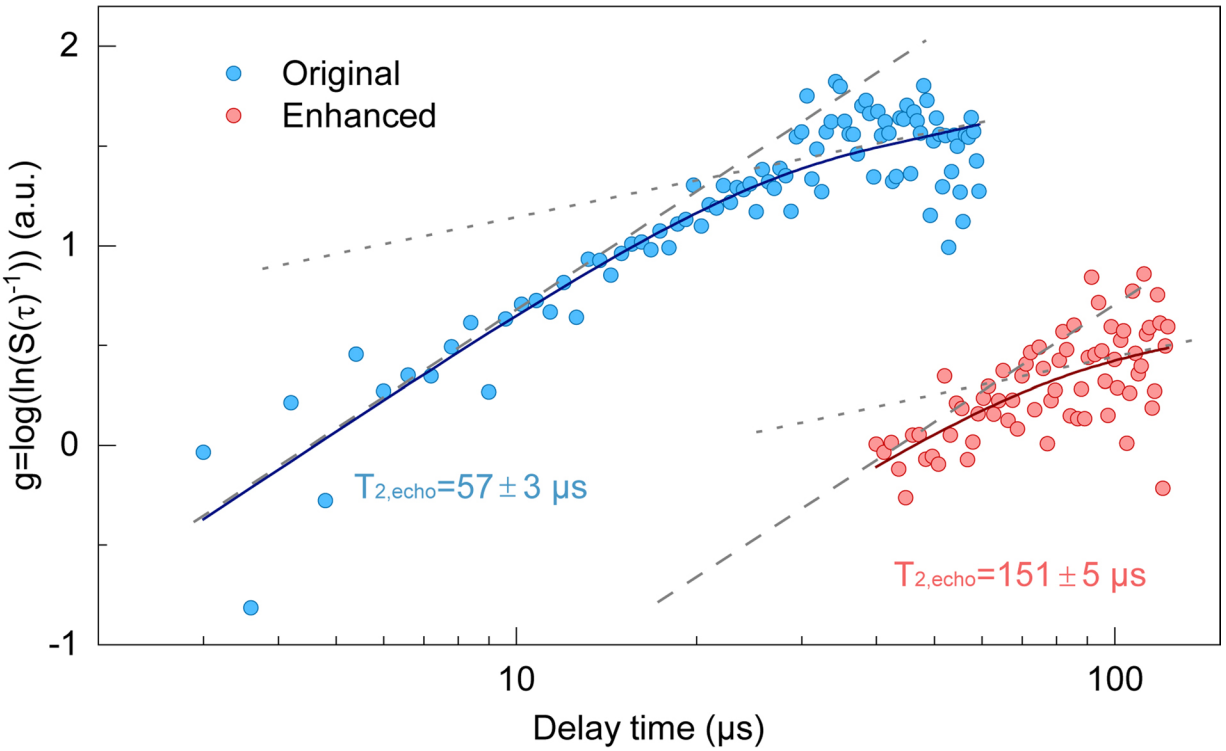

Extended Data Fig. 3 | Transition time in log-log plot of DEER spectra before and after the coherence enhancement. The DEER spectra of single NV demonstrated in the log-log plot showing the change of the transition time from ~21 μs to 64 μs before and after the charge manipulation. The coherence time was enhanced from 57 ± 3 μs up to 151 ± 5 μs. The dashed and dotted lines represent the powers of 2 and 2/3, respectively. In the model of configurational averaged surface spins, the transition time at which the DEER curve begins to demonstrate stretched exponential decay should be only sensitive to the depth of NV, regardless of the density of surface spins[34]. However, there should be subsurface electron spins such as P1 centre and charged vacancies induced by the ion implantation, which would also contribute to the decoherence and DEER signals of shallow NVs. Such subsurface spins may be located between the NV and the diamond surface, hence, the change of transition time indicates a changed distribution of the subsurface spins.

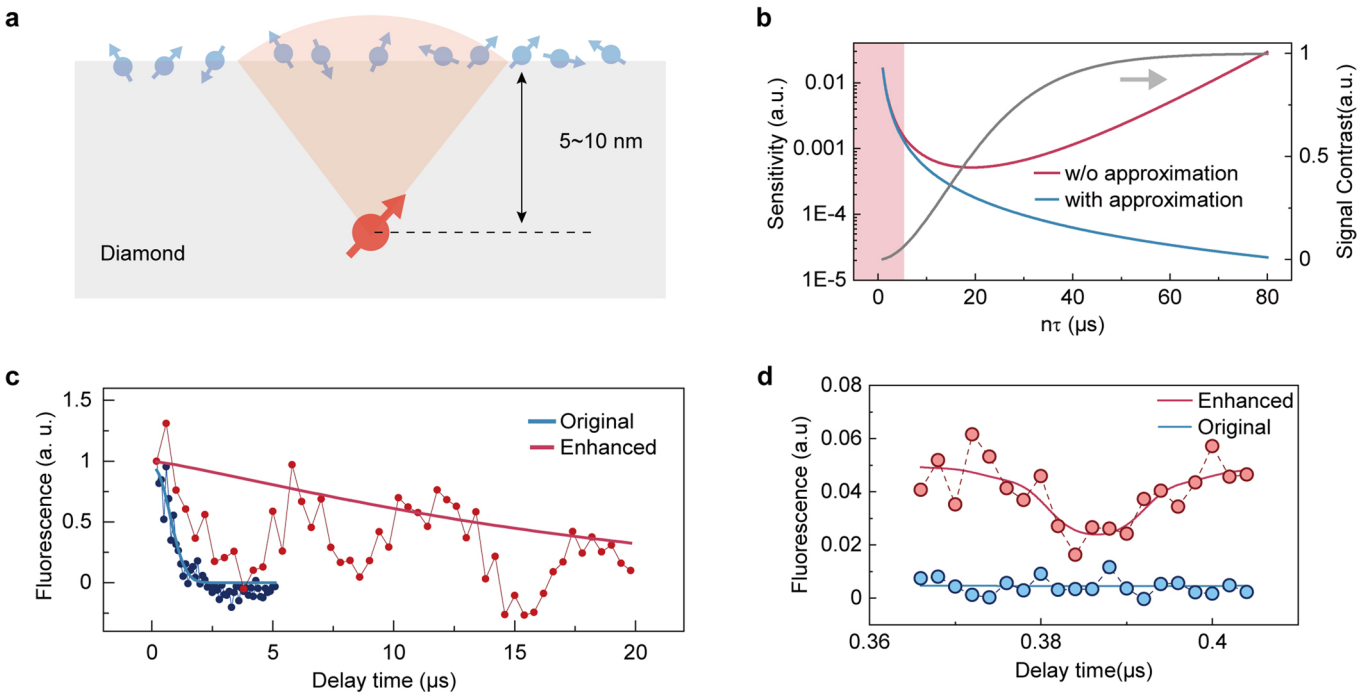

Extended Data Fig. 4 | Sensitivity enhancement for proton detection. a, Schematics showing the principle of detecting external protons by single NV centre. An ensemble of protons within the detecting volume (highlighted) contribute signals. **b**, The calculated sensitivity of single NV and its dependence on $n\tau$ according to the Equation 5. The detected field strength B^2_{rms} is chosen to be fitted from the red curve in **d**. The grey curve shows the corresponding signal contrast calculated by the Equation 4. The blue curve shows the sensitivity calculated based on the approximation of tiny signal contrast (Supplementary Text 5). Only within the region of small signal contrast (highlighted), the red and blue curve show good consistence. For simplicity, both the sensitivity and signal contrast were calculated by setting $C(n\tau)$=1. **c**, Spin-echo measurements of a very shallow NV showing T_2 enhancement of ~20 fold with our method. **d**, XY8-2 (blue curve) and XY8-12 (red curve) measurements of the same NV in **c** showing that after 'pull-and-push' method, such a quantum sensor with poor coherence can be used for detecting external protons, with the capability of detecting a minimum magnetic variance corresponding to ~0.18 protons. The red curve is offset for clarity. The external magnetic field is 303 Gauss.

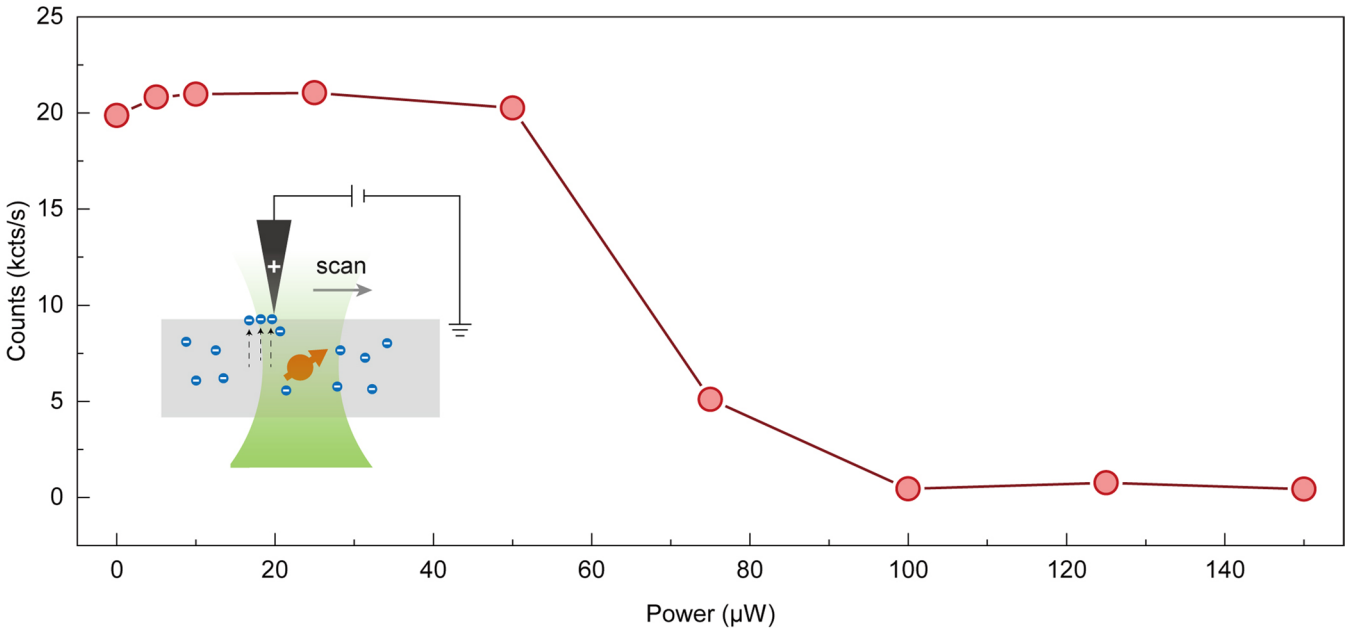

Extended Data Fig. 5 | Laser power dependence of surface polarization. The fluorescence of one shallow NV centre under varied laser power with tip bias of +50 V (red points). The NV^- completely coverts into NV^+ at ~100 μW, which can be considered as a criterion for the degree of surface polarization. Assuming that there is no geometric change in the gaussian-like focus spot at different laser power, this transition laser power can be used for the estimation of polarized area. For example, considering the typical size of our laser focus and the power used during the 'pulling' step, we can estimate a polarized area of ~ $265 \times 265\,nm^2$ under a laser power of ~300 μW and a tip bias of +50 V. Inset: the schematics showing the process of surface polarization described in Methods. When polarizing the surface, we fixed the laser focus on one NV centre and scanned the tip with positive bias around it.